



## Research Article

# Electrical and structural characterization of nano-carbon–aluminum composites fabricated by electro-charging-assisted process

X. Ge<sup>a</sup>, C. Klingshirn<sup>a</sup>, M. Morales<sup>a</sup>, M. Wuttig<sup>a</sup>, O. Rabin<sup>a, b</sup>, S. Zhang<sup>c</sup>, L.G. Salamanca-Riba<sup>a, \*</sup>

<sup>a</sup> Department of Materials Science and Engineering, University of Maryland, College Park, 20742, MD, USA

<sup>b</sup> Institute for Research in Electronics and Applied Physics, University of Maryland, College Park, 20742, MD, USA

<sup>c</sup> General Cable Indianapolis Technology Center, Indianapolis, IN, 46214, USA



## ARTICLE INFO

## Article history:

Received 2 June 2020

Received in revised form

19 October 2020

Accepted 20 October 2020

Available online 23 October 2020

## Keywords:

Nano-carbon

Aluminum/carbon composite

Microscopy

Spectroscopy

Electrical conductivity enhancement

## ABSTRACT

Incorporating nano-carbon phases into metal-matrix composites is a promising strategy for simultaneously enhancing electrical conductivity and mechanical properties of metals. Here, we describe the manufacture of novel nano-carbon-aluminum composites by an electro-charging-assisted process (EAP) that show  $5.6\% \pm 1.7\%$  increase in electrical conductivity compared to the base metal alloy. The source of nano-carbon that was used in this study is activated carbon with particle size less than 100 nm. The enhancement is attributed to nano-graphitic structures that extend through the lattice of the metal. Through electron transfer from the metal to the nano-structures the electron density at the interface of nano-crystalline graphite and the metal lattice increases thereby enhancing the bulk electrical conductivity. We identify the important fabrication parameters of the EAP for a reaction system employing a tapered graphite cathode. A high current density of 100 A/cm<sup>2</sup> causes ionization and crystallization of the carbon in the liquid metal. The increase in electrical conductivity of the composite is directly related to the incorporation of the nanocrystalline carbon in the metal lattice. The superior performance of these nano-carbon aluminum composites makes them promising candidates for power transmission lines and other applications.

© 2020 Elsevier Ltd. All rights reserved.

## 1. Introduction

The simultaneous improvement of the electrical conductivity and mechanical strength of metals has recently attracted much interest. Metal matrix composites produced with various forms of carbon inclusions are produced to benefit from the exceptional strength and charge carrier mobility of carbon nanostructures, such as graphene and carbon nanotubes (CNT) [1]. Nanocarbon metal matrix composites based on aluminum (Al) and its alloys have been widely investigated because of the many industrial applications of these low density metals with excellent mechanical properties, high electrical conductivity, and good processing performance. The investigations were successful in raising the metal's mechanical properties but spotty in increasing the electrical conductivity [2–9] with a few remarkable exceptions: Wang et al. [10] obtained a 4% increase in the electrical conductivity, 7.1% increase in the thermal

conductivity and 30% increase in the tensile strength of an Al/graphene composite with a carbon concentration of 0.5 wt% compared to the reference Al alloy with no carbon. However, in Al/graphene composites with carbon concentrations above 0.5 wt% both conductivities and the tensile strength decreased. The decrease was attributed to agglomeration of the graphene at grain boundaries. Similarly, Zhang, et al. [11] obtained a simultaneous increase in tensile strength (~17% increase) and electrical conductivity (2% increase) for Al/graphene composites fabricated by friction stir processing.

There are a number of obstacles to improving the electrical conductivity of Al alloys via nano-carbon incorporation: The agglomeration of graphene or CNT, increases the scattering of the charge carriers at the grain boundaries, hence reducing the conductivity [10,12,13]. Carbon or oxygen incorporation in aluminum can give rise to the formation of carbide or oxide which will likewise deteriorate the conductivity [10,12]. Most importantly, current techniques such as ball milling [14] and friction stir processing [11,13] are not compatible with scale-up manufacturing since they

\* Corresponding author.

E-mail address: [riba@umd.edu](mailto:riba@umd.edu) (L.G. Salamanca-Riba).

require either long time or multiple steps in processing.

In this paper, we report on an effort to produce aluminum-graphene composites using an industrially scalable electrocharging-assisted process (EAP). In this process, liquid aluminum and carbon precursors are mixed while a high current is passed through the liquid metal/carbon mixture. This method, initially developed by Third Millennium Materials, LLC (TMM) [15] has produced coherent metal-carbon composites, called “covetics” by the inventors, with increased electrical and/or thermal conductivity and tensile strength [16–22]. These samples showed coherent graphene nanoribbons epitaxially incorporated between (111) planes of the metal lattice [18,23]. It appears that both coherently and incoherently incorporated carbon nanostructures can increase the mechanical properties of the base metal or metal alloy, while only those nanostructures that are coherent with the metal matrix can potentially (also) increase the electrical conductivity.

Although enhanced electrical conductivity of covetics has been achieved, it is still difficult to consistently reproduce the improvement since the factors that contribute to better conductivity are nonetheless poorly understood. Additionally, non-uniform distribution of carbon is observed in current covetic samples, which in turn leads to non-uniformity in the properties of the material which has so far impeded their adoption by industry.

In the present work, we present a systematic investigation on the role of the EAP process parameters that control the incorporation of carbon in Al and the influence of carbon on the electrical conductivity of the composite. Through this study, we achieved Al–C composites with  $5.6\% \pm 1.7\%$  higher electrical conductivity and  $8.2\% \pm 6.7\%$  higher hardness compared to the parent Al alloy with no carbon. This improvement in conductivity is directly correlated to increase in crystallite size and content of the nano-carbon structures incorporated in the metal upon application of the current which had not been previously reported. The characterization of the composites by analysis of Raman scattering, XPS, TEM and XRD is presented in section 2. The role of the process parameters (reaction time, current density, and reaction volume) is presented in section 3. Section 4 describes the influences of nanocarbon crystallite size and content on the electrical conductivity of the composite. A detailed description of the sample preparation is provided in the supplementary section.

## 2. Characterization of covetics

The samples were prepared by EAP with in situ monitoring of current, voltage and temperature (full details of the fabrication process are provided in the Supplementary Information). In this study, we chose two types of carbon source: amorphous activated carbon with particle size less than 100 nm and graphite powder with particle size less than 45  $\mu\text{m}$ . Raman spectroscopy shows different signals for amorphous and graphitic carbon. The covetics conversion process converts amorphous carbon to extended graphitic (crystalline) structures. Thus, in order to observe this transition, we chose amorphous activated carbon as precursor in order to observe the increase in the crystallinity of the nano-carbon structures in the covetics, which indicates that the conversion process takes place as a result of the application of the current. In addition, activated carbon is very inexpensive which reduces the cost of the process. We also made samples with graphite powder to compare with samples made with activated carbon.

In a graphite crucible, nominal average concentrations of 3 wt % of activated carbon (or graphite powder) were added to the Al 1350 alloys. The mixture was placed in an induction furnace under continuous Ar flow. Once the Al melted, a mechanical stirrer was inserted into the liquid metal, and the mixture was stirred for 5 min to achieve a homogeneous Al–C mixture. Subsequently, a direct

current (DC) was applied to the molten mixture using a graphite rod inserted in the liquid as the cathode, and the graphite crucible as the anode. The current was applied in a constant current mode for a preset time. After the current was turned off, the cathode was removed from the liquid metal, the power to the furnace was turned off and the sample was allowed to cool and solidify gradually inside the crucible under continuous Ar flow. Two sets of samples were made in order to investigate the conversion of the Al/C mixture into a nano-carbon Al composite, i.e., the covetics conversion process. In series A, samples A1–A6 were prepared without stirring during the application of the current in order to qualitatively identify which parameters contribute significantly to the process. In series B, samples B1–B8 were prepared with continuous mixing, and the relevant parameters defined in series A were systematically varied in order to investigate the role of the size and content of the nanocarbon on the electrical conductivity of the composite. The fabrication details are described in the [Supplementary Information section S1.2](#).

Sample B1 showed the best electrical conductivity and highest increase in hardness. The characterization from this sample is presented here as an example to unveil the role of the parameters in the EAP process. Specimens from sample B1, cut from the region less than 0.5 cm from the electrode, were analyzed by Raman scattering, XRD, TEM and depth-profiling XPS.

Raman spectroscopy is highly sensitive to different types of carbon bonding, and has been widely used to identify different forms of carbon [24–26]. The so-called D and G peaks located around 1350 and 1580  $\text{cm}^{-1}$ , respectively, are peaks characteristic of graphitic materials corresponding to the breathing modes of  $\text{sp}^2$  rings, D and the  $\text{E}_{2g}$  phonon at the Brillouin zone center, G. The D peak is absent in perfect graphite and single layer graphene. It appears when symmetry breaking defects are introduced, such as at the edges of graphene or other graphitic defects (pentagons, heptagons, C vacancies, etc) [27,28]. Besides the D and G peaks, a peak observed at 2700  $\text{cm}^{-1}$ , called the 2D (or G') peak, is prominent in graphitic samples [28]. Raman spectra from the activated carbon source material used in this work show a very strong and broad D peak centered at  $\sim 1340 \text{ cm}^{-1}$  and a G peak at  $\sim 1595 \text{ cm}^{-1}$ , while the 2D peak is absent, Fig. 1 a). In contrast, the D peak position of samples processed with EAP decreased in intensity and the G-peak shifted to  $\sim 1585 \text{ cm}^{-1}$ , the position for graphite. The Raman spectrum of sample B1, representative of samples processed by EAP, is shown in Fig. 1 b). The D and G peaks are located at 1347  $\text{cm}^{-1}$  and 1580  $\text{cm}^{-1}$ , respectively; both in agreement with the D and G peak positions in graphite. The intensity of the D peak in sample B1 is much weaker relative to the G peak compared to the spectrum of activated carbon.

The ratio of the integrated intensities under the D and G-peaks,  $I_D/I_G$ , can be used to determine the crystallite size ( $L_a$ ) of graphitic nano-carbon, defined as the effective width of the basal plane [26,29], according to Eq. (1) [30]:

$$L_a(\text{nm}) = \frac{560}{E_l^4} \left( \frac{I_D}{I_G} \right)^{-1}, \quad (1)$$

where  $E_l$  is the laser excitation energy in eV (2.33 eV for a wavelength of 532 nm used in this work). In the first stage of a three-stage crystallization model [31], the value of  $L_a$  increases as the material becomes more crystalline. The analysis of sample B1 yielded  $L_a = 21.6 \pm 12.1 \text{ nm}$ . In contrast,  $L_a$  of the activated carbon precursor equaled only  $8.9 \pm 0.9 \text{ nm}$ . The blue shift of the G peak and increased  $L_a$  of carbon in covetics indicates that the amorphous carbon converted to nano-crystalline graphitic structures and extended networks upon the application of the current. Another

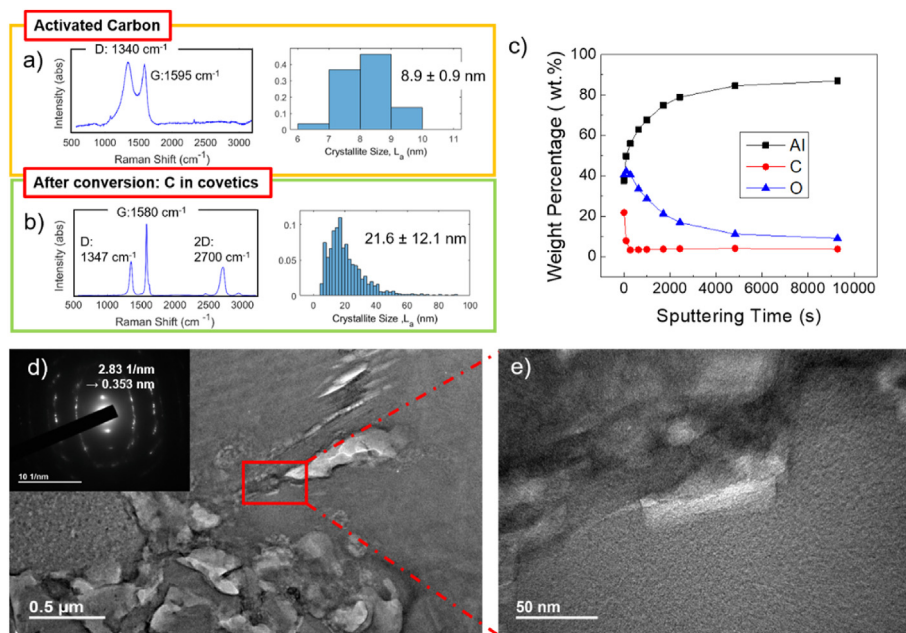


**Fig. 1.** Characterization of sample B1. a) Left: Typical Raman spectrum of activated carbon. Only the D and G peaks are present in the activated carbon (no 2D peak is present). Right: histogram of the nano-carbon crystallite size ( $L_a$ ) of activated carbon with an average of  $8.9 \pm 0.9$  nm. b) Left: Raman spectrum of the carbon observed in sample B1 after the EAP. The 2D peak appears at  $2700 \text{ cm}^{-1}$  and the G peak shifts to  $1580 \text{ cm}^{-1}$ , both of which agree with the 2D and G peak positions in graphite. Right: histogram of nano-carbon crystallite size ( $L_a$ ) in sample B1 with average of  $21.6 \pm 12.1$  nm. The increase of  $L_a$ , as well as the changes in the Raman spectrum (shifts of the D and G peaks and appearance of the 2D peak), indicate that the activated carbon converted to graphitic structures under the effect of the current. c) XPS depth profile of sample B1 showing local average C concentration of 4.0 wt % after 4 h of sputtering. d) Bright field TEM image of the C microstructure showing ordered regions on the order of microns, significantly larger than the activated C starting material, but also with local thickness variations and misorientation. Inset: electron diffraction pattern with spots corresponding to the c-axis interplanar spacing of graphite. e) High magnification of the region in the red box in d). (A colour version of this figure can be viewed online.)

indication of crystallization of the activated carbon is the appearance of the 2D peak at  $\sim 2700 \text{ cm}^{-1}$ , which is absent in the Raman spectra of activated carbon. Thus, we define carbon conversion in the covetics process as the formation of carbon with crystallite size above  $10.7 \text{ nm}$  (i.e., 2 standard deviations above the mean  $L_a$  for activated carbon) and a G peak at  $1580 \pm 5 \text{ cm}^{-1}$ . The presence of carbon in aluminum at high temperatures could give rise to the formation of aluminum carbide ( $\text{Al}_4\text{C}_3$ ) which is detrimental to the conductivity of the alloy. We note that the Raman spectrum of  $\text{Al}_4\text{C}_3$  presents a peak at around  $850 \text{ cm}^{-1}$  [32] which was not observed in any of the Raman spectra of samples processed by EAP, which indicates a hindrance of  $\text{Al}_4\text{C}_3$  formation in this process.

The XPS sputtering depth profile of sample B1, shown in Fig. 1 c), revealed 4 wt % carbon incorporation in the covetic. As expected, hydrocarbon contamination adsorbed on the surface of the sample resulted in high carbon concentration at the beginning of data collection. This signal tapered off to a consistent level representative of the bulk of the sample after  $\sim 2000$  s of sputtering time. Thus, the value of 4 wt% was obtained by averaging the integrated intensities under the C-1s, Al-2p and O-1s peaks in the XPS spectra using data collected at sputtering times longer than 2000 s. The measured carbon content was higher than the nominal 3 wt % added in sample B1 indicative of a non-uniform carbon distribution in the sample.

XRD analysis (not shown) indicated that both the grain size and the lattice constant of the Al matrix were reduced in the covetic sample compared to the parent Al 1350, as indicated by the peak positions and full width at half maximum (FWHM) in the XRD spectra. The Al crystallite size of sample B1 and Al 1350 reference equaled  $183 \pm 12 \text{ nm}$  and  $245 \pm 52 \text{ nm}$ , respectively. The Al lattice constants of sample B1 and parent Al 1350 derived from XRD equaled  $0.40392 \pm 0.00009 \text{ nm}$  and  $0.40441 \pm 0.00004 \text{ nm}$ , respectively, indicating a slight contraction of the lattice upon

carbon incorporation. The decrease of the Al lattice constant in the covetic can be attributed to the Al (111)/C (0001) plane epitaxy reported in covetics [18]. No peak corresponding to the  $\text{Al}_4\text{C}_3$  was detected in the X-ray diffraction spectra (not shown). These results agree with those previously reported for Al6061 covetics with nominally 5 wt % C [33].

A cross-sectional TEM specimen was prepared by FIB from a region of sample B1 where graphitic ordering was observed via Raman spectroscopy (average  $L_a = 21.6 \pm 12.1 \text{ nm}$ ). This region contained a large inclusion of C which had been converted from disordered activated C to graphitic C as shown in Fig. 1 d) and e). Graphitic ordering is indicated by the electron diffraction pattern in the inset of Fig. 1 d), which shows spots with an interplanar spacing of  $0.35 \text{ nm}$  corresponding to the c-axis interplanar spacing of graphite. The regions of graphitic ordering extend for a few microns, one order of magnitude larger than the particle diameter of the activated C source material. On a larger scale, thickness variations and misorientation of graphitic structures persist, contributing to the ring-like features of the diffraction pattern (inset to Fig. 1 d)). Again, no traces of aluminum carbide have been detected in the course of our TEM studies. Clusters of carbon in the range from a few hundred nm to tens of microns were observed from TEM images and Raman spectroscopy maps.

### 3. The role of process parameters on the covetics conversion process

In this study, six samples, A1 to A6 were prepared (without stirring during the application of the current) to identify the main factors that contribute to the covetics conversion process. The parameters that were varied were: reaction time,  $t_r$ , reaction volume,  $V_r$ , and current density. Previous studies have shown that  $100 \text{ A/cm}^2$  is a critical current density required to initiate the covetics

conversion process [33]. The region of the sample that experiences a current density above a critical current density, i.e., where the conversion process takes place, is defined as the reaction volume,  $V_r$ . The time that the carbon is being exposed to the critical current density is defined as reaction time,  $t_r$ . Raman and XPS measurements were performed to elucidate the covetics conversion process. Raman spectra were collected over areas of  $10\ \mu\text{m} \times 10\ \mu\text{m}$  in mapping mode across the cross section of the sample. The spectra were analyzed by a MATLAB based nonlinear iterative fitting algorithm [34]. This analysis provides the fraction of graphitic carbon in the sample,  $G\%$ , estimated as the fraction of Raman spectra that show crystallite size  $L_a > 10.7\ \text{nm}$  (i.e., nano-carbon crystallite size larger than that for the activated carbon source). Together with the total carbon concentration,  $C_T$ , measured from XPS depth profile, we estimated the concentration of graphitic carbon in the metal matrix  $G_C = C_T \times G\%$ .

### 3.1. Effects of reaction time $t_r$

In order to understand the contribution from the reaction time, five samples (samples A1–A5) were prepared with different  $t_r$ , i.e., 2, 5, 10, 15 and 30 min (Fig. 2 a) and Table 1). (Fabrication details are described in Supplementary Information section S1.2) Fig. 2 b) shows the current density distribution inside the crucible simulated by finite element analysis (COMSOL). The calculation shows that for a tapered graphite electrode, the current density distribution is highly non-uniform. It decays below  $100\ \text{A}/\text{cm}^2$  at a distance

of about 0.4 cm from the tip of the electrode. Based on the simulation, two samples were collected for Raman and XPS analysis in two regions from cross-sections of each disk. Region R1 was a 1 cm wide slab containing the region with current density above  $100\ \text{A}/\text{cm}^2$  while region R2 was a 1 cm wide slab cut from an area more than 4 cm from the electrode as shown in Fig. 2 b).

The results of the Raman and XPS measurements are compiled in Table 1. The data demonstrate that during the first 2 min of current flow the total and graphitic carbon concentrations in both region R1 and region R2 remained largely unchanged. After applying the current for longer than 5 min, higher total and graphitic carbon concentrations were detected in the region R1 than in the region R2. Overall, the content of graphitic carbon,  $G_C$  in the region R1 increases linearly as a function of reaction time,  $t_r$ , while the content of graphitic carbon,  $G_C$  from region R2 did not change significantly (Fig. 2c), indicating that the current attracts the carbon towards the electrode. The carbon, then, crystallizes under the high current density and incorporates in the metal matrix upon solidification.

The average crystallite size,  $L_a$ , of carbon measured from samples collected in region R1 increases as a linear function of  $t_r$  (Fig. 2d) and Table 1). However,  $L_a$  determined from region R2 is similar to that of activated carbon ( $\sim 10\ \text{nm}$ ) regardless of  $t_r$  demonstrating that temperature alone is not enough to induce crystallization of the carbon. The G peak position of samples extracted in region R1 shifts from  $1588\ \text{cm}^{-1}$  to  $1580\ \text{cm}^{-1}$  as  $t_r$  increases from 2 min to 30 min. In contrast, the G peak positions of

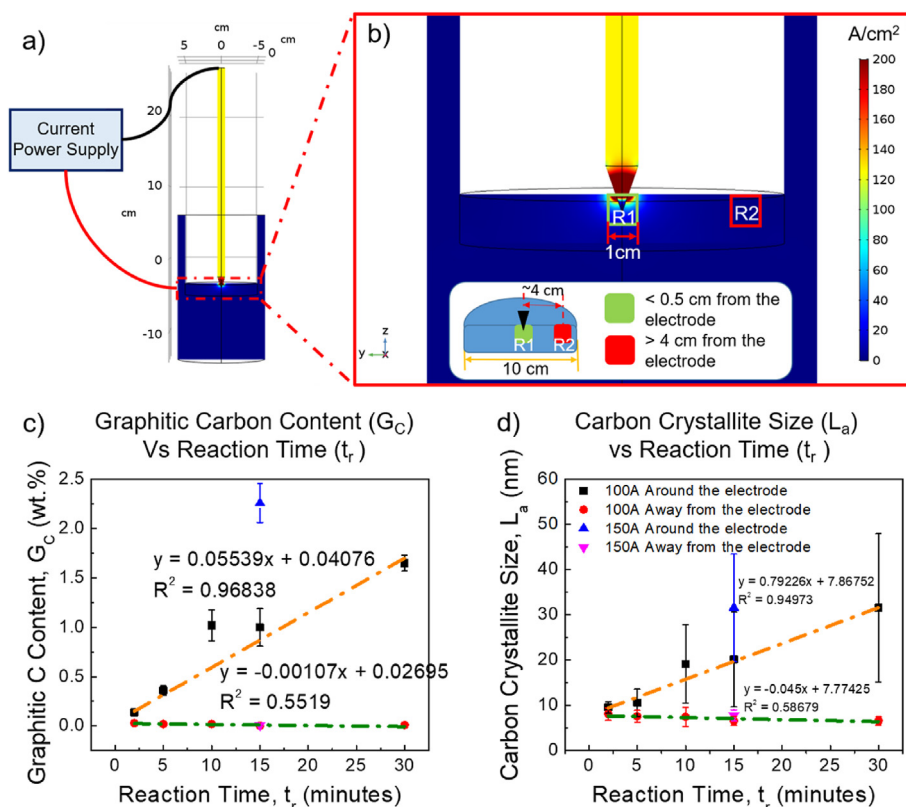


**Fig. 2.** a) Schematic of the experiment for samples A1–A6. The sharpened graphite electrode was stationary at the center of the crucible for the duration of the reaction. b) COMSOL simulation of the current density distribution around the tip of the cathode. The region of maximum current density is localized within a hemisphere of 0.4 cm radius around the cathode. Inset to b) Cross-section of the sample after sectioning to indicate the regions of the sample that were analyzed (positions 1 and 2). Region R1 (in green rectangle) was chosen from the region within 0.5 cm around the electrode, while region R2 (in red rectangle) was more than 4 cm away from the electrode. c) The graphitic carbon concentration,  $G_C$ , in region R1 increases linearly with reaction time,  $t_r$ , while  $G_C$  in region R2 did not change with  $t_r$ . d) The crystallite size of carbon,  $L_a$ , in region R1 increases linearly with  $t_r$ , while it remains independent of  $t_r$  in region R2. (A colour version of this figure can be viewed online.)

**Table 1**  
Summary of different fabrication conditions and XPS and Raman results for samples A1–A6.

Sample Number	Current (A)	Reaction Time, $t_r$ (mins)	Position from cathode	Crystallite Size, $L_a$ (nm)	Graphitic Fraction, G %	Total C, $C_T$ (wt.%)	Graphitic C, $G_C$ (wt.%)	G peak Position ( $\text{cm}^{-1}$ )
A1	100 A	2 min	R1	$9.6 \pm 1.3$	$18 \pm 9\%$	$0.8 \pm 0.1$	$0.1 \pm 0.02$	$1588.2 \pm 6.0$
			R2	$8.1 \pm 1.4$	$5 \pm 4\%$	$0.6 \pm 0.1$	$0.03 \pm 0.003$	$1592.3 \pm 5.3$
A2	100 A	5 min	R1	$10.6 \pm 3.0$	$33 \pm 3\%$	$0.9 \pm 0.1$	$0.4 \pm 0.05$	$1584.2 \pm 7.9$
			R2	$7.6 \pm 1.3$	$3 \pm 2\%$	$0.7 \pm 0.1$	$0.02 \pm 0.004$	$1596.4 \pm 4.3$
A3	100 A	10 min	R1	$19.2 \pm 8.7$	$74 \pm 1\%$	$1.4 \pm 0.2$	$1.0 \pm 0.2$	$1582.9 \pm 6.6$
			R2	$7.5 \pm 2.1$	$4 \pm 3\%$	$0.7 \pm 0.1$	$0.02 \pm 0.001$	$1600.1 \pm 4.9$
A4	100 A	15 min	R1	$20.2 \pm 10.5$	$86 \pm 4\%$	$1.2 \pm 0.2$	$1.0 \pm 0.2$	$1579.5 \pm 6.2$
			R2	$6.6 \pm 1.0$	$1 \pm 1\%$	$0.5 \pm 0.1$	$0.005 \pm 0.001$	$1594.5 \pm 7.1$
A5	100 A	30 min	R1	$31.6 \pm 16.4$	$94 \pm 2\%$	$1.8 \pm 0.1$	$1.7 \pm 0.1$	$1576.7 \pm 7.1$
			R2	$6.6 \pm 0.9$	$3 \pm 2\%$	$0.7 \pm 0.2$	$0.01 \pm 0.003$	$1595.0 \pm 4.1$
A6	150 A	15 min	R1	$31.6 \pm 11.9$	$95 \pm 0.6\%$	$2.4 \pm 0.2$	$2.3 \pm 0.2$	$1579.2 \pm 3.7$
			R2	$7.8 \pm 1.2$	$5 \pm 3\%$	$0.7 \pm 0.1$	$0.007 \pm 0.0004$	$1592.1 \pm 4.6$

samples from region R2 remain in the range of  $1590\text{--}1600\text{ cm}^{-1}$ , the same as for activated carbon. This result is in agreement with Ferrari's stage 2 of a three-stage model where the carbon transitions from amorphous carbon to nano-crystalline graphite; namely, the crystallite size of carbon increases and the G peak position shifts from  $\sim 1600\text{ cm}^{-1}$  to  $1580\text{ cm}^{-1}$  [27,31]. During too short processing time,  $t_r$ , the activated carbon does not have sufficient time to rearrange into nano-crystalline graphitic structures. Only longer exposure to current density above  $100\text{ A/cm}^2$  in the region R1 gives rise to crystallite growth and the formation of ordered nano-crystalline graphitic carbon in the metal matrix. For the carbon in the region R1, and  $t_r \geq 10$  min, the average crystallite size becomes larger than that of activated carbon, the G peak position blue-shifts from  $1590$  to  $1580\text{ cm}^{-1}$ , and the 2D peak appears in the Raman spectra. Thus, for the tapered graphite cathode and an applied current of  $100\text{ A}$ , the minimum reaction time,  $t_r$  to crystallize activated carbon to nano-crystalline graphitic carbon is  $10$  min. It follows that longer exposure to the current density  $\geq 100\text{ A/cm}^2$  gives rise to crystallite growth and the formation of more ordered nano-crystalline graphitic carbon in the metal matrix.

### 3.2. Effects of reaction volume $V_r$

To estimate  $V_r$ , Raman scattering was performed on five specimens cut from sample A4 (samples A4 a–e) as illustrated in Fig. 3 a).

The width of each sample was  $\sim 1\text{ cm}$ . Raman results are collected in Table 2. As the table shows at distances from  $0.5\text{ cm}$  to  $4.5\text{ cm}$  from the electrode, the G peak positions shift to higher wavenumber and the crystallite size of carbon decreases profoundly. Only sample A4-a, closest to the electrode, presents larger crystallite size than that of activated carbon, while samples A4 b–e all have similar crystallite size to that of activated carbon. Similarly, only the G peak position of carbon in sample A4-a equals that of graphite; the G peak positions of the other samples are all similar to activated carbon. As indicated in Table 2, G% decreases for the samples cut farther away from the electrode. As shown in Fig. 3 b), the current density in the region within  $0.4\text{ cm}$  of the electrode (sample A4-a) is above  $100\text{ A/cm}^2$ , which facilitates crystallization of the carbon into nano-crystalline graphitic structures. Beyond  $0.4\text{ cm}$  from the electrode, the current density drops below the critical current density for crystallization and the carbon remains as activated carbon [33]. We define  $V_r$  as the volume of the sample exposed to a current density above  $100\text{ A/cm}^2$  where there is significant increase of the nano-carbon crystallite size. Hence, the current density distribution simulated by COMSOL bestows  $V_r$  for different geometries of the cathode. For the tapered graphite cathode, and  $100\text{ A}$  applied current,  $V_r$  for covetics conversion corresponds to a hemisphere of  $0.4\text{-cm}$  radius around the electrode. In order to complete the conversion from activated carbon to nano-crystalline graphite, the activated carbon should reside within  $V_r$ .

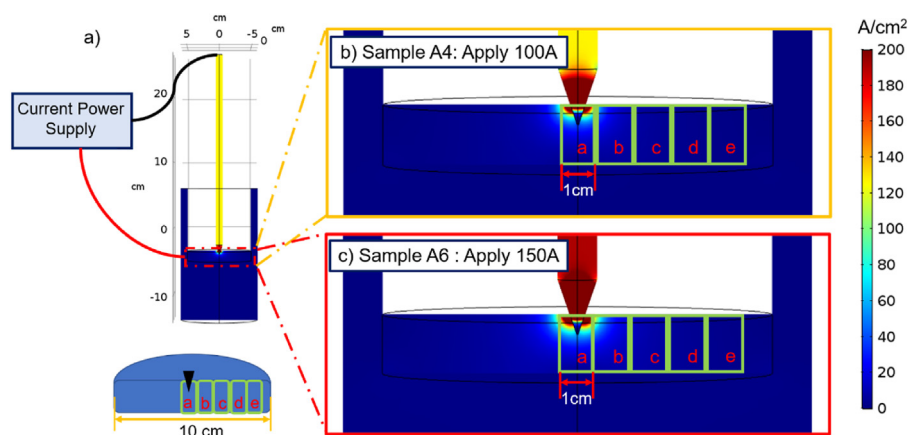


**Fig. 3.** Schematics of sample location for investigation of reaction volume,  $V_r$ . a) Top; the graphite electrode was kept stationary at the center of the crucible for the duration of the reaction. Bottom; samples a–e were taken in steps of  $1\text{ cm}$  from  $0\text{ cm}$  to  $4.0\text{ cm}$  away from the electrode. The width of each sample is  $1\text{ cm}$ . b) COMSOL simulation of current density distribution of sample A4 with  $100\text{ A}$  applied current. The volume of critical current density is a hemisphere of radius  $0.4\text{ cm}$  around the tip of the electrode. The current density beyond this region decreases abruptly. c) COMSOL simulation of current density distribution of sample A6 at  $150\text{ A}$ . The region of critical current density extends to a wider range compared with  $V_r$  in sample A4 for  $100\text{ A}$  current. (A colour version of this figure can be viewed online.)

**Table 2**  
Summary of conditions and Raman scattering results for samples A4 a-e.

Sample Number	Sample Position	Crystallite Size, $L_a$ (nm, average)	Graphitic C Fraction, G %	G peak Position ( $\text{cm}^{-1}$ )	2D peak Position ( $\text{cm}^{-1}$ )	Current density ( $\text{A}/\text{cm}^2$ , left to right)
A4-a	Around Electrode (0 → 0.5 cm)	$20.2 \pm 10.5$	$86 \pm 4\%$	$1579.5 \pm 6.2$	$2702.5 \pm 9.4$	$3102 \rightarrow 100$
A4-b	1 cm Away (0.5 → 1.5 cm)	$7.3 \pm 1.6$	$7 \pm 3\%$	$1591.5 \pm 5.5$	N/A	$100 \rightarrow 11$
A4-c	2 cm Away (1.5 → 2.5 cm)	$7.2 \pm 1.0$	$2 \pm 2\%$	$1591.3 \pm 6.2$	N/A	$11 \rightarrow 5.5$
A4-d	3 cm Away (2.5 → 3.5 cm)	$7.5 \pm 1.3$	$4 \pm 3\%$	$1594.9 \pm 6.3$	N/A	$5.5 \rightarrow 3.0$
A4-e	4 cm Away (3.5 → 4.5 cm)	$6.5 \pm 1.0$	$1 \pm 1\%$	$1594.5 \pm 7.1$	N/A	$3.0 \rightarrow 1.4$

### 3.3. Effects of current density

Sample A6 was prepared with the same  $t_r = 15$  min as sample A4 but with a higher current of 150A. Five samples A6 a-e were obtained similar to samples A4 a-e in order to investigate the effect of current density on carbon crystallization and integration. The analyses of the Raman spectra are collected in Table 3. In sample.

A6-a,  $L_a$  in the region less than 0.5 cm from the electrode equals  $31.6 \pm 11.9$  nm, which is much larger than  $L_a$  in sample A4-a ( $20.2 \pm 10.5$  nm) at 100A for  $t_r = 15$  min. In sample A6-a,  $G_C = 2.3 \pm 0.2$  wt%, which is more than the  $G_C$  in sample A4-a ( $G_C = 1.0 \pm 0.2$  wt%) as shown in Fig. 2 c). As indicated in Table 3, the carbon found in the region 1.5 cm from the electrode (sample A6-b) still reveals some growth of nano-crystalline carbon and a higher G% than in sample A4-b.  $t_r$  for both samples A4 and A6 was the same, but the current applied in sample A6 was higher than the current applied in sample A4. As shown in Fig. 3 c), both maximum current density and  $V_r$  in sample A6 are larger than in sample A4 (Fig. 3b)). Furthermore, sample A5 was prepared with lower current (100A) but two times longer  $t_r$  than sample A6.  $L_a$  in the region R1 in sample A6, for 150A and  $t_r = 15$ min, is approximately the same as  $L_a$  in the region R1 in sample A5 for 100A and  $t_r = 30$  min (see Fig. 2 d)). Also, Fig. 2 c) indicates that the region R1 of sample A6 has more graphitic carbon than the same region in sample A4. Thus, applying higher current increases the current density, consequently  $V_r$  also increases so that the covetics conversion process takes place in a larger volume, producing more graphitic carbon structures with larger crystallite size that integrate with the metal matrix in a shorter  $t_r$ .

## 4. Electrical conductivity of covetics

The results presented in section 3 indicate that to complete the covetics conversion process, the activated carbon particles need to be exposed to a critical current density ( $>100 \text{ A}/\text{cm}^2$ ) for sufficient time  $t_r$ . Samples B1–B8 were prepared to investigate the role of  $L_a$  and  $G_C$  on the electrical conductivity of covetics. Samples B7 and B8 are reference samples with no carbon. The fabrication conditions are summarized in Table 4. (The details of fabrication conditions are

**Table 3**  
Summary of conditions and Raman scattering results for samples A6 a-e.

Sample Number	Sample Position	Crystallite Size, $L_a$ (nm, average)	Graphitic C Fraction, G %	G peak Position ( $\text{cm}^{-1}$ )	2D peak Position ( $\text{cm}^{-1}$ )	Current density ( $\text{A}/\text{cm}^2$ , left to right)
A6-a	Around Electrode (0 → 0.5 cm)	$31.6 \pm 11.9$	$95 \pm 0.6\%$	$1579.2 \pm 3.7$	$2706.0 \pm 9.6$	$4666 \rightarrow 175$
A6-b	1 cm Away (0.5 → 1.5 cm)	$13.2 \pm 7.8$	$25 \pm 4\%$	$1579.6 \pm 8.6$	$2702.2 \pm 23.8$	$175 \rightarrow 16$
A6-c	2 cm Away (1.5 → 2.5 cm)	$8.4 \pm 1.2$	$5 \pm 4\%$	$1592.5 \pm 3.4$	N/A	$16 \rightarrow 8.2$
A6-d	3 cm Away (2.5 → 3.5 cm)	$8.0 \pm 1.3$	$5 \pm 3\%$	$1591.7 \pm 7.3$	N/A	$8.2 \rightarrow 4.6$
A6-e	4 cm Away (3.5 → 4.5 cm)	$7.9 \pm 1.3$	$5 \pm 3\%$	$1592.1 \pm 4.6$	N/A	$4.6 \rightarrow 2.0$

described in the Supplementary Information section S1.2.) Raman scattering, XPS and electrical conductivity measurements were performed on all the samples; the results are presented in Table 5.

### 4.1. Effect of crystallite size of carbon, $L_a$ on the conductivity of covetics

Fig. 4 a) displays the correlation between electrical conductivity and nano-carbon crystallite size,  $L_a$ . As discussed in section 2, the increase of carbon crystallite size,  $L_a$  corresponds to the transition from amorphous activated carbon to nano-crystalline graphitic carbon. The larger crystallite size of carbon indicates an increasingly ordered network of nano-crystalline graphite. The corresponding G peak positions of samples B1–B5 in Table 4, are all similar to that of graphite confirming the presence of nano-crystalline graphite in all the samples. The correlation revealed in Fig. 4 a) and b) demonstrates that nano-crystalline graphite formed during the conversion process gives rise to improvement in electrical conductivity of covetics compared to the control sample B7. Also, larger crystallite size correlates with higher electrical conductivity. Thus, it is important to incorporate nano-crystalline graphite with large crystallite size in the matrix of the metal to enhance electrical conductivity of covetics.

The porosity of the samples was similar for the covetics and the reference samples with slightly higher values for the covetic samples. The samples with lowest porosity (samples B1 and B4) have the highest electrical conductivity values. However, samples B2 and B5 have higher porosity than that of the reference sample, but they still demonstrate better electrical conductivity than the reference sample, indicating that covetics have the potential for improving electrical conductivity even further once voids are eliminated from the sample through processing.

### 4.2. Effect of Al–C interface in covetics

The discussion above demonstrates that larger crystallite size of nano-crystalline graphite enhances the electrical conductivity. In order to achieve larger crystallite size of carbon in covetics, we used  $45 \mu\text{m}$  in diameter graphite powder particles as precursor to

**Table 4**  
Summary of different fabrication conditions for samples B1–B8.

Sample Number	Carbon Source	Carbon Particle Size ( $\mu\text{m}$ )	Electrode Geometry	Applied Current (A)	Reaction Time, $t_r$ (s)	Maximum Current Density ( $\text{A}/\text{cm}^2$ )
B1	Activated Carbon	<0.1	Tapered	100	1000	3102
B2	Activated Carbon	<0.1	Tapered	100	360	3102
B3	Activated Carbon	<0.1	Cu electrode w/Graphite sheath	150	1000	49
B4	Activated Carbon	<0.1	Cu electrode w/Graphite sheath	200	1000	65
B5	Activated Carbon	<0.1	Three Parallel electrodes	200	2000	280
B6	Graphite Powder	45	Tapered	100	1000	3102
B7	N/A	N/A	N/A	N/A	N/A	N/A
B8	N/A	N/A	Tapered	100	1000	3102

**Table 5**  
Summary of XPS, Raman scattering and electrical conductivity results of samples B1–B8.

Sample Number	Total C, $C_T$ (wt.%)	Graphitic C Fraction, G% (wt.%)	Graphitic Carbon, $G_C$ (wt.%)	Volume Fraction of Graphitic C (vol. %)	Porosity (%)	Nano-C Crystallite Size, $L_a$ (nm)	Electrical Conductivity ( $\times 10^7$ , S/m)	Electrical Conductivity (% IACS)
B1	$4.0 \pm 0.2$	$91 \pm 3\%$	$3.6 \pm 0.2$	$4.3 \pm 0.2$	$0.6 \pm 0.2$	$21.6 \pm 12.0$	$3.57 \pm 0.02$	$61.8 \pm 0.7$
B2	$2.2 \pm 0.3$	$39 \pm 3\%$	$0.9 \pm 0.1$	$1.0 \pm 0.1$	$1.6 \pm 0.6$	$10.5 \pm 3.2$	$3.43 \pm 0.02$	$59.2 \pm 0.7$
B3	$2.5 \pm 0.6$	$53 \pm 2\%$	$1.3 \pm 0.3$	$1.5 \pm 0.3$	$0.7 \pm 0.2$	$16.6 \pm 11.7$	$3.45 \pm 0.02$	$59.8 \pm 0.7$
B4	$4.4 \pm 0.2$	$80 \pm 2\%$	$3.5 \pm 0.1$	$4.0 \pm 0.1$	0	$19.0 \pm 8.8$	$3.55 \pm 0.02$	$61.3 \pm 0.7$
B5	$2.9 \pm 0.1$	$95 \pm 0.3\%$	$2.7 \pm 0.1$	$3.3 \pm 0.2$	$2.9 \pm 1.0$	$29.5 \pm 15.2$	$3.49 \pm 0.02$	$60.3 \pm 0.7$
B6	$9.1 \pm 0.7$	N/A	$9.1 \pm 0.7$	$11.0 \pm 0.9$	$1.2 \pm 0.4$	$77.3 \pm 27.4$	$3.43 \pm 0.02$	$59.0 \pm 0.7$
B7	N/A	N/A	N/A	N/A	$0.9 \pm 0.3$	N/A	$3.36 \pm 0.02$	$58.4 \pm 0.7$
B8	N/A	N/A	N/A	N/A	$1.7 \pm 0.6$	N/A	$3.39 \pm 0.02$	$58.6 \pm 0.7$

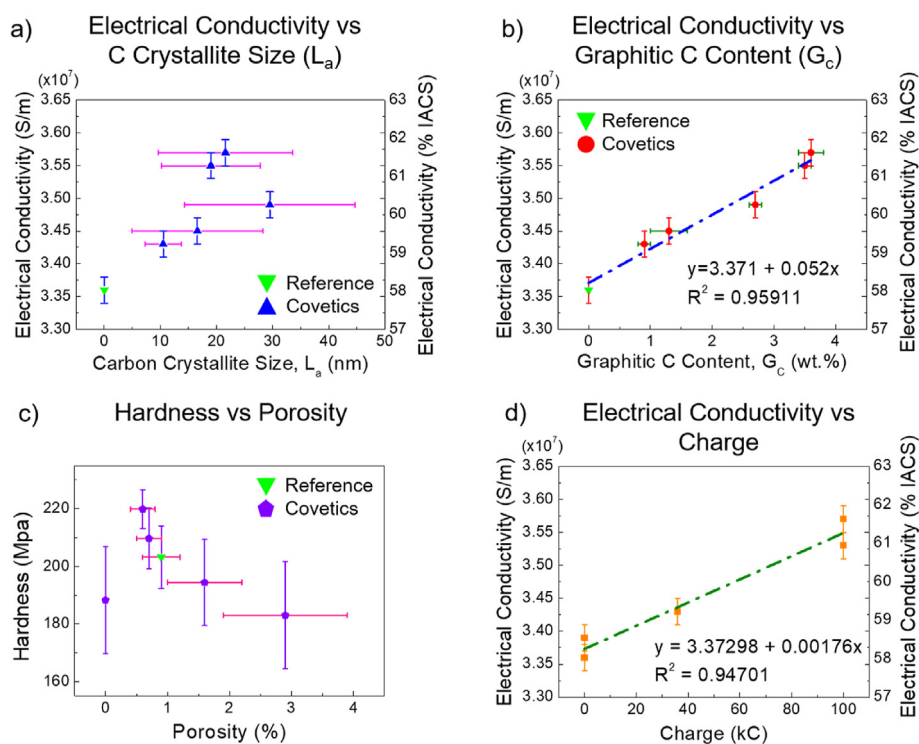


**Fig. 4.** Enhanced electrical conductivity of covetics is positively correlated with the nano-carbon crystallite size ( $L_a$ ), concentration of graphitic carbon ( $G_C$ ) and the total charge imparted during the reaction. a) The electrical conductivity of covetics as a function of nano-carbon crystallite size,  $L_a$ . The larger crystallite size of carbon gives rise to higher electrical conductivity of covetics. The outlier in this figure for  $L_a = 30$  nm, is due to lower converted carbon in the sample. b) Electrical conductivity as function of graphitic carbon content,  $G_C$ . Higher graphitic carbon in covetics results in higher electrical conductivity due to more graphitic structures and Al–C interfaces in the sample. c) Except for sample B4 with no porosity, there is a trend that the hardness increases with decreased porosity in the sample. d) The electrical conductivity of covetics as function of total charge,  $Q_T = I \times t_r$ , infused during the reaction. (A colour version of this figure can be viewed online.)

prepare sample B6. The Raman spectra indicated after conversion a nano-carbon crystallite size of  $77.3 \pm 27.4$  nm in sample B6, much larger than the crystallite size of samples B1–B5 made from

activated carbon as source. However, the electrical conductivity of sample B6 was only  $3.34 \times 10^7$  S/m, lower than those of samples B1–B5 suggesting that crystallite size of the nano-carbon is not

enough to increase electrical conductivity.

It is known that doped multilayer graphene with metal contacts results in an increase in carrier density in the nano-graphitic structures and the electron transfer is restricted to the two layers of graphene in epitaxial contact with the metal. Additional graphitic layers do not contribute to the conductivity enhancement [35]. The covetics conversion process creates interfaces between Al and nano-carbon which enable electron transfer from Al to the graphitic structures [36], [37]. We conclude that the electron transfer effect improves the electrical conductivity of covetics. However, in sample B6, the graphite powder has many layers of nano-crystalline carbon, but only the two layers at the top and bottom contribute to enhancing electrical conductivity even though the carbon crystallite size,  $L_a$ , is much larger than for activated carbon. Therefore, it is essential to form many interfaces between nano-crystalline graphite and the Al matrix in addition to increasing  $L_a$  to improve the electrical conductivity of covetics.

#### 4.3. Effect of graphitic carbon content, $G_C$ , on the electrical conductivity of covetics

Fig. 4 b) shows that the electrical conductivity depends linearly on the graphitic carbon concentration,  $G_C$  in addition to  $L_a$ . Although the crystallite size of the nano-carbon in sample B5 ( $L_a = 29.5 \pm 15.2$  nm) is larger than those in samples B1 ( $L_a = 21.6 \pm 12.0$  nm) and B4 ( $L_a = 19.0 \pm 8.8$  nm), the electrical conductivity is lower for sample B5 than for samples B1 and B4 because  $G_C$  is lower in sample B5 ( $G_C = 2.7$  wt%) compared to 3.6 and 3.5 wt% for samples B1 and B4, respectively. This observation reveals that the conductivity not only depends on the crystallite size of the nano-carbon, but also relies on the concentration of nano-crystalline graphite present in the metal. Thus, it is necessary to incorporate sufficient nano-crystalline carbon in the metal matrix to improve the electrical conductivity of the composite.

### 5. Mechanical properties

The hardness of samples B1–B8 was examined using indentation to explore the role of carbon on the mechanical properties of covetics. Data were collected from each sample in five positions along the length and on both sides of the samples to get an average value. The hardnesses of samples B1 and B7 (reference) are  $219.87 \pm 6.8$  MPa, and  $203.20 \pm 10.9$  MPa, respectively, representing  $8.2\% \pm 6.7\%$  enhancement of the covetic compared to the reference sample. This enhancement is a consequence of the incorporation of graphitic structures in the Al matrix and the resulting stress fields hindering the dislocation motion [10]. Currently, we do not do any post treatments on our samples, which gives rise to porosity in the sample. The hardness measurements have a large error due to the porosity of the samples. Fig. 4 c) indicates a trend that samples with lower porosity exhibit higher hardness (except for sample B4 with no porosity), which shows the potential that the hardness can be further improved if voids can be eliminated through processing. Future work will investigate if there is a clear dependence of hardness with graphitic carbon content, once the voids are eliminated from the sample.

### 6. Discussion

We propose that there are two important factors that give rise to improved electrical conductivity in covetics. First, graphene or graphitic structures with  $sp^2$  bonding should be present in the form of nano-carbon graphitic networks with few impurities and defects, in order to preserve the intrinsically high charge carrier mobility of these nanostructures. Second, large number of

interfaces between Al and C should exist in the composite which give rise to electron donation from Al to the nano-crystalline graphite and improvement of the electrical conductivity of the composite.

As shown in Fig. 4 a), the positive correlation between electrical conductivity and nano-carbon crystallite size,  $L_a$ , indicates that larger crystallite size of carbon is needed in order to preserve the high electron mobility of graphitic structures, for instance by minimizing the concentration of scattering sites.

Fig. 4 b) demonstrates that the electrical conductivity also increases as more graphitic carbon,  $G_C$ , is incorporated in the metal matrix. Higher concentration of graphitic carbon results in more nano-crystalline graphite integration in the Al matrix and more interfaces between Al and C, both of which proved essential for improving electrical conductivity. Our studies indicate that both longer reaction time,  $t_r$ , and higher current density induce larger nanocarbon crystallite size incorporation in the matrix of the metal during the EAP of covetics. Larger reaction volume,  $V_r$ , increases the likelihood of carbon being converted to nano-crystalline graphitic carbon and reduces the reaction time,  $t_r$ , to complete the conversion process as well. The latter is valuable for cost-effectiveness of the process of covetics at industrial manufacturing levels.

The enhancement of the electrical conductivity of covetics depends critically on the covetics conversion process to create a network of nano-crystalline graphite with adequate interfaces between Al and C in the metal matrix that extends throughout the sample. This can be achieved through the application of a high current density ( $>100$  A/cm<sup>2</sup>), over a large reaction volume,  $V_r$ , for sufficient reaction time,  $t_r$ . The five samples depicted in Fig. 4 d) show an increase in electrical conductivity compared to the reference (pure Al 1350) sample as a function of total charge imparted during the reaction. Longer reaction time allows activated carbon to rearrange into more ordered graphitic structures with larger crystallite size. A higher applied current produces larger reaction volume receiving higher current density which facilitates the growth of nano-crystalline graphitic structures over a larger volume.

Conductivity enhancements depend on the nature of the starting materials used to fabricate the covetics. Using 45  $\mu$ m graphite particles (sample B6) with an average nano-carbon crystallite size of 200–400 nm (instead of 100 nm activated carbon particles with  $L_a$  10 nm) induced a decrease of the conductivity. We observed that in this case the EAP process reduced the crystallite size,  $L_a$ , to 80 nm. Since it is known that only the top two layers adjacent to the metal contribute to the enhancement [35] the additional layers for thicker graphite particles will not receive electrons from the metal and would in turn decrease the conductivity. It is still possible that graphite powder can be used as the source of carbon in covetics. However, the parameters controlling the incorporation of graphite powder into covetics would need to be reinvestigated.

The enhancement of the electrical conductivity in covetics is inconsistent with the rule of mixtures based on non-interactive components. This rule approximates the conductivity of a composite,  $\sigma_c$ , as a volume-weighted average of the conductivities of the matrix ( $\sigma_m$ ) and its aligned uniaxial inclusions ( $\sigma_f$ ). Under this model, the conductivity should lie between the lower bound set by the loading (i.e., the applied voltage) transverse to the orientation of the inclusions (Reuss model [38]) and the upper bound set by the case where the loading is applied along the inclusion axis (Voigt model [39]). This is described by

$$\left(\frac{f}{\sigma_f} + \frac{1-f}{\sigma_m}\right)^{-1} \ll \sigma_c \ll f\sigma_f + (1-f)\sigma_m \quad (2)$$

where  $f$  is the volume fraction of the inclusion.

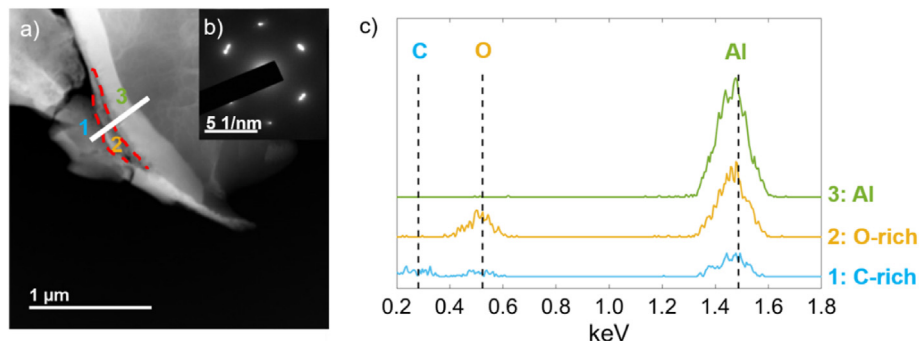


**Fig. 5.** Analysis of Al–C interface by (S)TEM and energy-dispersive X-ray spectroscopy (EDS). a) HAADF-STEM image (Z-contrast) showing a band between Al and C. b) Diffraction pattern from the area shown in a), with a hexagonal bright pattern of spots corresponding to the Al (110) plane. c) Selected spectra from EDS line scan across the interfaces (white line in a)), spaced 200 nm apart. From bottom to top: 1) C-rich phase also containing Al, followed by 2) an oxygen-rich phase (probably aluminum oxide), and 3) pure Al matrix. (A colour version of this figure can be viewed online.)

The electrical conductivity of Al 1350 is about  $3.8 \times 10^7$  S/m [40]. This value is larger than conductivities reported for graphitic structures such as pure graphite ( $2 \times 10^6$  S/m [41]) or even suspended graphene ( $\sim 2.2 \times 10^7$  S/m [42]). Therefore,  $\sigma_c$  is expected to always be smaller than  $\sigma_m$  for any volume fraction of carbon  $f$  greater than zero, as long as the assumptions implied by the rule of mixtures are valid – chiefly that the inclusions and the matrix are non-interacting. This assumption appears not to be valid for covetics because several samples showed conductivity enhancement.

The electrical conductivity enhancement we observe can be qualitatively interpreted if the graphitic structures created by the EAP introduce graphene into the Al matrix. When nano-crystalline graphitic structures are in good ohmic contact with the Al matrix, electrons transfer from Al to the graphitic structures to equilibrate the Fermi level, since the work function of Al is higher than that of graphene [36]. Thus, the electron density at the interfaces between the graphitic structures and Al increases. Together with the intrinsically high electron mobility of graphitic structures ( $2 \times 10^5$  cm<sup>2</sup>/Vs for graphene [42]), the electrical conductivity of bulk covetics increases. The fabrication condition of sample B1 represents the optimum combination of all three factors which produced the best electrical conductivity among all the samples. These conditions formed a network of extended graphitic structures inside the liquid Al with sufficiently high quality to maintain a high electron mobility to improve the overall conductivity of the composite. In addition, the nano-crystalline graphitic structures are homogeneously dispersed inside the sample and possess good electrical contact with the metal host. Nevertheless, an atomic-scale theoretical study is necessary to confirm the role of graphitic nanostructures on the electrical conductivity of Al–C composites made by EAP.

The one-step EAP method can avoid introducing defects and contaminants in the composite, which make it more suitable for large scale production and processing. Wang et al., reported 4% enhancement in the electrical conductivity and 44% improvement in the hardness of Al-graphene composites with addition of 0.5 wt% graphene. However, both electrical conductivity and hardness decreased when carbon concentration increased beyond 0.5 wt% due to agglomeration of the graphene at grain boundaries [10]. In our work, covetics with addition of 4 wt% carbon to Al 1350 demonstrated simultaneous improvement of  $5.6\% \pm 1.7\%$  in the electrical conductivity and  $8.2\% \pm 6.7\%$  in hardness compared to the pure Al 1350 alloy. The carbon in covetics is homogeneously distributed in the Al matrix with less agglomeration, at least on the centimeter scale, confirmed by Raman spectroscopy. These improvements reflect enhancement of the electrical conductivity

above other composites made by techniques, such as ball milling [10] and friction stir processing [11], which indicate that EAP is a viable fabrication method to produce Al–C composites with better electrical conductivity.

The interface quality between the Al matrix and incorporated C nanostructures is especially significant to conductivity enhancement in covetics. Increases in electrical resistance at these interfaces diminish the conductivity enhancement of the bulk composite. To investigate this interface in detail, a TEM specimen was prepared from sample B1 using ion milling to provide a larger area that is more representative of the overall sample. It revealed regions containing Al and graphitic structures that were qualitatively similar; one such region is shown in Fig. 5. The high angle annular dark field (HAADF) STEM image in Fig. 5 a) suggests a band between the Al matrix and incorporated C which is composed of C, interfacial aluminum oxide, followed by pure Al matrix (Fig. 5 c) proceeding from left (spectrum 1) to right (spectrum 3) in Fig. 5a), respectively. The 200 nm wide O- rich region will have a locally detrimental effect on electrical conductivity between Al and incorporated C by preventing the C phase from carrying current and contributing to conductivity enhancement [36]. It is important to note that, again, no evidence for aluminum carbide was seen in covetics, either by TEM, XRD, or Raman spectroscopy. The presence of oxides in this sample suggests that further conductivity enhancement will be possible in covetics, if oxygen can be eliminated from the system during fabrication.

## 7. Conclusions

In summary, we successfully fabricated Al 1350 nano-carbon metal composites, called covetics, with  $5.6\% \pm 1.7\%$  enhanced electrical conductivity and  $8.2\% \pm 6.7\%$  improved hardness compared to the base aluminum alloy. The improved electrical and mechanical properties are attributed to high quality interfaces between Al and nano-crystalline graphitic structures in the composite. Our results highlight the fabrication conditions to form crystalline graphitic nano-carbon by EAP featuring a tapered graphite cathode: high current with density above 100 A/cm<sup>2</sup> and a reaction time,  $t_r$ , of 10 min or longer. Processing under these conditions creates many interfaces between Al and the nano-graphitic structures, which in turn gives rise to improved electrical conductivity of the composite. The composites showed some formation of aluminum oxide which is expected to detrimentally affect the overall conductivity. Thus, future work will focus on improvements in processing methods to prevent oxygen incorporation and void formation in the samples, which should give rise to further increase

in the conductivity of these materials. We would like to investigate if there is a clear dependence of hardness with graphitic carbon content once the samples are free of voids. We will also study possible galvanic corrosion issues of aluminum covectics for future manufacturing and commercialization. We believe Al 1350 covectics with excellent electrical and mechanical performance could potentially replace Cu with Al alloys and/or other metals in many applications. More broadly, the fabrication methods described in this paper can be applied to other metal and metal alloy systems.

## Disclaimer

This work was prepared as an account of work sponsored by an agency of the United States Government. Neither the United States Government, nor any agency thereof, nor any of their employees, makes any warranty, expressed or implied, or assumes any legal liability or responsibility for the accuracy, completeness, or usefulness of any information, apparatus, product, or process disclosed, or represents that its use would not infringe privately owned rights. Reference herein to any specific commercial product, process, or service by trade name, trademark, manufacturer, or otherwise does not necessarily constitute or imply its endorsement, recommendation, or favoring by the United States Government or any agency thereof. Any findings, opinions, and conclusions or recommendations expressed in this report are those of the authors and do not necessarily reflect those of the United States Government or any agency thereof.

## CRediT authorship contribution statement

**X. Ge:** was the main contributor to the work. This manuscript is based on her PhD thesis. **C. Klingshirn:** Formal analysis, performed analysis of Raman scattering data and TEM analysis. **M. Morales:** performed some of the Raman scattering electrical conductivity measurements. **M. Wuttig:** Formal analysis, contributed with discussions and analysis of the data. **O. Rabin:** Formal analysis, contributed with discussions and analysis of the data. **S. Zhang:** performed electrical conductivity and hardness measurements of the composites Lourdes Salamanca-Riba is the principal investigator of the project.

## Declaration of competing interest

The authors declare that they have no known competing financial interests or personal relationships that could have appeared to influence the work reported in this paper.

## Acknowledgments

This work was supported in part by ANL/DOE under contract 6F-30062 and the U. S. Department of Energy under Award No. EE0008313; Dr. Tina Kaarsberg is the Project Technology Manager and Debbie Schultheis is the Project Officer/Manager. We acknowledge the use of the TEM and FIB/SEM at the University of Maryland Nanocenter and its AIM Laboratory.

## Appendix A. Supplementary data

Supplementary data to this article can be found online at <https://doi.org/10.1016/j.carbon.2020.10.063>.

## References

- [1] X. Zhang, N. Zhao, C. He, The superior mechanical and physical properties of nanocarbon reinforced bulk composites achieved by architecture design - a review, *Prog. Mater. Sci.* 113 (2020). AUG 2020.
- [2] Q. Liu, L. Ke, F. Liu, C. Huang, L. Xing, Microstructure and mechanical property of multi-walled carbon nanotubes reinforced aluminum matrix composites fabricated by friction stir processing, *Mater. Des.* 45 (2013) 343–348. MAR 2013.
- [3] Behzad Sadeghi, Pasquale Cavaliere, Ghasem Azimi Roeeen, Martin Nosko, Morteza Shamanian, Veronika Trembošová, Stefan Nagy, N. Ebrahimzadeh, Hot rolling of MWCNTs reinforced Al matrix composites produced via spark plasma sintering, *Advanced Composites and Hybrid Materials 2* (2019) 549–570.
- [4] X. Gao, H. Yue, E. Guo, H. Zhang, X. Lin, L. Yao, B. Wang, Preparation and tensile properties of homogeneously dispersed graphene reinforced aluminum matrix composites, *Mater. Des.* 94 (2016) 54–60. MAR 15 2016.
- [5] Farhad Saba, Seyed Abdolkarim Sajjadi, Simin Heydari, Mohsen Haddad-Sabzevar, Jaafar Salehi, H. Babayi, A novel approach to the uniformly distributed carbon nanotubes with intact structure in aluminum matrix composite, *Advanced Composites and Hybrid Materials 2* (2019) 540–548.
- [6] C. He, N. Zhao, C. Shi, X. Du, J. Li, H. Li, Q. Cui, An approach to obtaining homogeneously dispersed carbon nanotubes in Al powders for preparing reinforced Al-matrix composites, *Adv. Mater.* 19 (8) (2007) 1128–1132. APR 20 2007.
- [7] A. Esawi, K. Morsi, A. Sayed, M. Tahera, S. Lanka, Effect of carbon nanotube (CNT) content on the mechanical properties of CNT-reinforced aluminium composites, *Compos. Sci. Technol.* 70 (16) (2010) 2237–2241. DEC 31 2010.
- [8] M. Bastwros, G. Kim, C. Zhu, K. Zhang, S. Wang, X. Tang, X. Wang, Effect of ball milling on graphene reinforced Al6061 composite fabricated by semi-solid sintering, *Compos. B Eng.* 60 (2014) 111–118. APR 2014.
- [9] Z. Liu, B. Xiao, W. Wang, Z. Ma, Singly dispersed carbon nanotube/aluminum composites fabricated by powder metallurgy combined with friction stir processing, *Carbon* 50 (5) (2012) 1843–1852. APR 2012.
- [10] J. Wang, L. Guo, W. Lin, J. Chen, C. Liu, S. Chen, S. Zhang, T. Zhen, Effect of the graphene content on the microstructures and properties of graphene/aluminum composites, *N. Carbon Mater.* 34 (3) (2019) 275–285. JUN 2019.
- [11] S. Zhang, G. Chen, T. Qu, G. Fang, S. Bai, Y. Yan, G. Zhang, Z. Zhou, J. Shen, D. Yao, Y. Zhang, Q. Shi, Simultaneously enhancing mechanical properties and electrical conductivity of aluminum by using graphene as the reinforcement, *Mater. Lett.* 265 (2020). APR 15 2020.
- [12] C. Xu, B. Wei, R. Ma, J. Liang, X. Ma, D. Wu, Fabrication of aluminum-carbon nanotube composites and their electrical properties, *Carbon* 37 (5) (1999) 855–858, 1999.
- [13] Z. Liu, B. Xiao, W. Wang, Z. Ma, Tensile strength and electrical conductivity of carbon nanotube reinforced aluminum matrix composites fabricated by powder metallurgy combined with friction stir processing, *J. Mater. Sci. Technol.* 30 (7) (2014) 649–655. JUL 2014.
- [14] M. Hahm, J. Nam, M. Choi, C. Park, B. Cho, S. Kazunori, Y. Kim, D. Kim, M. Endo, D. Kim, R. Vajtai, P. Ajayan, S. Song, Low interfacial contact resistance of Al-graphene composites via interface engineering, *Nanotechnology* 26 (21) (2015). MAY 29 2015.
- [15] J. V. Shugart, and R. C. Scherer, "USA Patent 8349759, 2013".
- [16] D.R. Forrest, I. Jasiuk, L. Brown, P. Joyce, A. Mansour, L.G. Salamanca-Riba, Novel metal-matrix composites with integrally-bound nanoscale carbon, 2012, pp. 560–563.
- [17] Lloyd Brown, Peter Joyce, David Forrest, L. Salamanca-Riba, Physical and mechanical characterization of a nanocarbon infused aluminum-matrix composite 3 (1) (2014).
- [18] H. Jaim, R. Isaacs, S. Rashkeev, M. Kuklja, D. Cole, M. LeMieux, I. Jasiuk, S. Nilufar, L. Salamanca-Riba, Sp(2) carbon embedded in Al-6061 and Al-7075 alloys in the form of crystalline graphene nanoribbons, *Carbon* 107 (2016) 56–66. OCT 2016.
- [19] B. Ma, J. Wang, T. Lee, S. Dorris, J. Wen, U. Balachandran, Microstructural characterization of Al4C3 in aluminum-graphite composite prepared by electron-beam melting, *J. Mater. Sci.* 53 (14) (2018) 10173–10180. JUL 2018.
- [20] Mete Bakir, I. Jasiuk, Novel Metal-Carbon Nanomaterials: A Review on Covectics, 2017, pp. 884–890.
- [21] R. Isaacs, H. Jaim, D. Cole, K. Gaskell, O. Rabin, L. Salamanca-Riba, Synthesis and characterization of copper-nanocarbon films with enhanced stability, *Carbon* 122 (2017) 336–343. OCT 2017.
- [22] R. Isaacs, H. Zhu, C. Preston, A. Mansour, M. LeMieux, P. Zavalij, H. Jaim, O. Rabin, L. Hu, L. Salamanca-Riba, Nanocarbon-copper thin film as transparent electrode, *Appl. Phys. Lett.* 106 (19) (2015). MAY 11 2015.
- [23] L. Salamanca-Riba, R. Isaacs, M. LeMieux, J. Wan, K. Gaskell, Y. Jiang, M. Wuttig, A. Mansour, S. Rashkeev, M. Kuklja, P. Zavalij, J. Santiago, L. Hu, Synthetic crystals of silver with carbon: 3D epitaxy of carbon nanostructures in the silver lattice, *Adv. Funct. Mater.* 25 (30) (2015) 4768–4777. AUG 12 2015.
- [24] M. Dresselhaus, A. Jorio, M. Hofmann, G. Dresselhaus, R. Saito, Perspectives on carbon nanotubes and graphene Raman spectroscopy, *Nano Lett.* 10 (3) (2010) 751–758. MAR 2010.
- [25] A. Ferrari, J. Meyer, V. Scardaci, C. Casiraghi, M. Lazzeri, F. Mauri, S. Piscanec, D. Jiang, K. Novoselov, S. Roth, A. Geim, Raman spectrum of graphene and graphene layers, *Phys. Rev. Lett.* 97 (18) (2006) 187401 (1-4), NOV 3 2006.
- [26] A. Ferrari, J. Robertson, Raman spectroscopy of amorphous, nanostructured, diamond-like carbon, and nanodiamond, *Phil. Trans. Math. Phys. Eng. Sci.* 362 (1824) (2004) 2477–2512. NOV 15 2004.
- [27] C. Casiraghi, A. Hartschuh, H. Qian, S. Piscanec, C. Georgi, A. Fasoli,

- K. Novoselov, D. Basko, A. Ferrari, Raman spectroscopy of graphene edges, *Nano Lett.* 9 (4) (2009) 1433–1441. APR 2009.
- [28] L. Malard, M. Pimenta, G. Dresselhaus, M. Dresselhaus, Raman spectroscopy in graphene, *Physics Reports-Review Section of Physics Letters* 473 (5–6) (2009) 51–87. APR 2009.
- [29] F. Tuinstra, J. Koenig, Raman spectrum of graphite, *J. Chem. Phys.* 53 (3) (1970) 1126, 1970.
- [30] L. Cancado, K. Takai, T. Enoki, M. Endo, Y. Kim, H. Mizusaki, A. Jorio, L. Coelho, R. Magalhaes-Paniago, M. Pimenta, General equation for the determination of the crystallite size  $L_a$  of nanographite by Raman spectroscopy, *Appl. Phys. Lett.* 88 (16) (2006) 163106 (1–3), APR 17 2006.
- [31] A. Ferrari, J. Robertson, Interpretation of Raman spectra of disordered and amorphous carbon, *Phys. Rev. B* 61 (20) (2000) 14095–14107. MAY 15 2000.
- [32] L. Yolshina, R. Muradymov, I. Korsun, G. Yakovlev, S. Smirnov, Novel aluminum-graphene and aluminum-graphite metallic composite materials: synthesis and properties, *J. Alloys Compd.* 663 (2016) 449–459. APR 5 2016.
- [33] X. Ge, C. Klingshirn, M. Wuttig, K. Gaskell, P. Zavalij, Y. Liang, C. Shumeyko, D. Cole, L. Salamanca-Riba, Mechanism studies and fabrication for the incorporation of carbon into Al alloys by the electro-charging assisted process, *Carbon* 149 (2019) 203–212. AUG 2019.
- [34] T.C. O'Haver, A pragmatic introduction to signal processing with applications in scientific measurement. <https://terpconnect.umd.edu/~toh/spectrum/index.html>.
- [35] M. Cao, D. Xiong, L. Yang, S. Li, Y. Xie, Q. Guo, Z. Li, H. Adams, J. Gu, T. Fan, X. Zhang, D. Zhang, Ultrahigh electrical conductivity of graphene embedded in metals, *Adv. Funct. Mater.* 29 (17) (2019). APR 25 2019.
- [36] M. Cao, Y. Luo, Y. Xie, Z. Tan, G. Fan, Q. Guo, Y. Su, Z. Li, D. Xiong, The influence of interface structure on the electrical conductivity of graphene embedded in aluminum matrix, *Advanced Materials Interfaces* 6 (13) (2019). JUL 2019.
- [37] G. Giovannetti, P. Khomyakov, G. Brocks, V. Karpan, J. van den Brink, P. Kelly, Doping graphene with metal contacts, *Phys. Rev. Lett.* 101 (2) (2008). JUL 11 2008.
- [38] A. Reuss, Berechnung der Fließgrenze von Mischkristallen auf Grund der Plastizitätsbedingung für Einkristalle, *ZAMM - Zeitschrift für Angew. Math. und Mech* 9 (1) (1929) 49–58.
- [39] W. Voigt, Ueber die Beziehung zwischen den beiden Elasticitätsconstanten isotroper Körper, *Ann. Phys.* 274 (12) (1889) 573–587.
- [40] R.A. Serway, *Principles of Physics*, second ed., Saunders College Pub, Fort Worth, 1998, p. 602.
- [41] P. Wallace, The band theory of graphite, *Phys. Rev.* 71 (9) (1947) 622–634, 1947.
- [42] K. Bolotin, K. Sikes, Z. Jiang, M. Klima, G. Fudenberg, J. Hone, P. Kim, H. Stormer, Ultrahigh electron mobility in suspended graphene, *Solid State Commun.* 146 (9–10) (2008) 351–355. JUN 2008.